Amirhossein Salimi[1]
Mem. ASME
Department of Mechanical Engineering,
University of Houston,
Houston, TX 77004
e-mail: asalimi@uh.edu

Amin Ramezanifar
Mem. ASME
Department of Mechanical Engineering,
University of Houston,
Houston, TX 77004
e-mail: aramezanifar@uh.edu

Javad Mohammadpour[2]
Mem. ASME
College of Engineering,
The University of Georgia,
Athens, GA 30602
e-mail: javadm@uga.edu

Karolos M. Grigoriadis
Mem. ASME
Department of Mechanical Engineering,
University of Houston,
Houston, TX 77004
e-mail: karolos@uh.edu

Nikolaos V. Tsekos
Department of Computer Science,
University of Houston,
Houston, TX 77004
e-mail: nvtsekos@uh.edu

Design and Qualification of a Parallel Robotic Platform to Assist With Beating-Heart Intracardiac Interventions

Using robotic systems to assist with sophisticated medical interventions such as aortic valve replacement under beating heart conditions necessitates the development of dexterous manipulators to ensure a safe and reliable operation. These mechanisms should not only be capable of tracking the desired trajectories with a high level of accuracy but also need to cope with strict medical constraints such as environment compatibility, patient safety and compactness. In this paper, we propose to design and experimentally qualify a robotic platform that takes into account the aforementioned requirements. Benefiting from the features of a parallel architecture, this four degrees of freedom (DOF) magnetic resonance imaging (MRI)-compatible patient-mounted and cable-driven manipulator (ROBOCATHETER) seeks to steer cardiac catheters under beating heart condition, while suitably addressing the deficiencies that currently used manipulators vastly suffer from. In addition to the detailed description of the robot design and its dedicated power transmission system, we also present the derivation of the robot's forward and inverse kinematic equations. The control algorithm implemented for the system actuation is a varying-gain proportional-integral-derivative (PID) controller, whose tracking performance will be examined. [DOI: 10.1115/1.4026334]

1 Introduction and Motivation for This Work

Design and experimental validation of robotic manipulator-based platforms to assist with MRI-guided surgical procedures have been examined over the past decade. These procedures cover a wide range of operations from neurosurgery [1] to prostate needle placement [2]. Recently, trans-apical approach for performing beating-heart interventions has attracted the attention of many researchers. This approach significantly reduces the side effects in cardiopulmonary bypass procedures and results in a faster patient recovery [3]. The results of using an MRI-guided robotic system for trans-apical aortic valve implantation under beating-heart condition are reported in Ref. [4]. Later, this system was integrated with a novel pneumatically actuated valve delivery module and its performance was evaluated through ex-vivo experiments in Ref. [5]. In a parallel study, a conceptual system design aimed for robot assisted MRI-guided aortic valve replacement was proposed in Ref. [6]. Focusing on beating-heart procedures, the authors in latter studies proposed to use MRI for guiding robotic manipulators in sophisticated heart surgeries. The objective of the present study is to propose an MRI-compatible robotic platform that can assist with aortic valve implantation under beating-heart conditions. To accomplish this goal as described in Ref. [6] and depicted in Fig. 1, if the catheter passes through the apex and the steering point, the aorta would be accessible simply by bending the proximal part of the tool. The insertion and bending part is handled by another mechanism, whose description and functionality is not within the scope of this paper. The interested reader is referred to Ref. [7] for the design and analysis of this module. The current platform objective is to sought to steer the catheter such that it would passes through the apex and steering point.

Considering the existing challenges in the design and operation of the aforementioned systems, the proposed mechanism is aimed to improve the quality of such robotic procedure. To make the actuation system MRI-compatible, several solutions have been proposed in the literature. Manual actuation [8], use of hydraulic cylinders [9], and utilizing pneumatic systems as the source of actuation [10] are some of the alternatives for magnetic motors for this purpose. Some of the major drawbacks of implementing these methods include lack of precise navigation, fluid leakage in cylinders and limited stiffness of motors as the consequence of air compressibility [11]. Most of the recent MRI-compatible actuation systems utilize piezoelectric motors, in which motion is produced through the vibration of piezoelectric ceramics. Although these motors are magnet-free, image artifacts are observed due to the high frequency electric currents [12]. To avoid the aforementioned issues, in this study, we use conventional electric motors and place them far from the sensitive areas to make ROBOCATHETER fully MRI-compatible. In order to transfer the generated torque to the robot's joints, a cable transmission system is proposed and implemented. The proposed system configuration allows each link to be actuated in both directions only by reversing the rotation in the corresponding motors.

While the design and qualification of patient-mounted robotic platforms for MRI-guided interventions have been previously examined for applications such as percutaneous needle placement [13], to the best of our knowledge, no such system has been so far introduced for intracardiac interventions in the literature.

[1]Corresponding author.
[2]Previously with University of Houston.

Contributed by the Mechanisms and Robotics Committee of ASME for publication in the Journal of Mechanisms and Robotics. Manuscript received September 5, 2012; final manuscript received November 23, 2013; published online March 4, 2014. Assoc. Editor: Philippe Wenger.

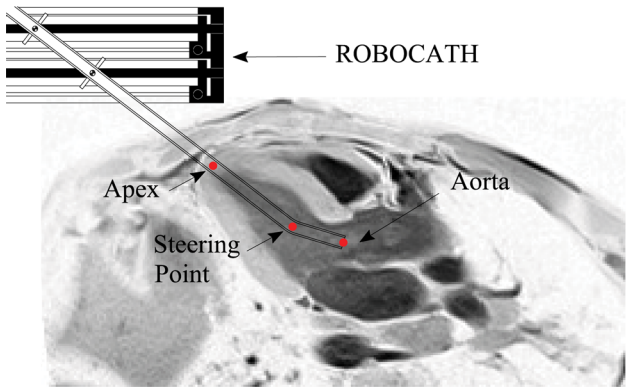

Fig. 1 Landmarks used in reaching aortic annulus

Mounting the platform on the patient not only helps the system cope with relative chest motion with respect to the fixed frames but also achieves compactness of the design. This is accomplished by restricting the platform size and eliminating the need of large links stretching from the patient's chest to the manipulator base outside the MRI bore. In this paper, we first describe the proposed design of the mechanism and the transmission system. Then, we present the derivation of the forward kinematics of the manipulator, as well as the inverse kinematic equations to allow for tracking of any arbitrary trajectories inside the workspace (in our case left ventricle (LV)). This section is followed by the development of an experimental test bed to examine the actuation of all the DOF associated with the manipulator by utilizing four DC motors controlled using a variable-gain PID controller. The results demonstrate the successful trajectory tracking of ROBOCATHETER which is essential to successfully perform aortic valve implantation procedure. Our other studies of ROBOCATHETER are as follows. The design and control of a haptic device for teleoperation of the catheter was investigated in Ref. [14]. The actuation of the platform using stepper motors was investigated [15]. In Ref. [16], ROBOCATHETER was used in a master–slave configuration. In Ref. [17], a model-based control of the system was studied, using a gain-scheduling approach.

2 Design of the Platform

In this section, we describe the details involved in the design and actuation of ROBOCATHETER. The objective is to design a mechanism that allows in-plane positioning and orientation of the catheter's tip, which necessitates the development of a 5-DOF manipulator. However, since the end effector is axisymmetric, one DOF could be omitted leading to a 4-DOF mechanism. The proposed design is partly inspired by earlier works in Refs. [18,19]. To further enhance the performance of these systems and to develop a robotic platform that is highly-customized for an operation such as aortic valve implantation, the proposed platform has a cylindrical structure and uses journal bearings in the rotational motion to reduce friction. It also employs a cable-driven force transmission system to make the actuation system MRI compatible. Furthermore, it is patient-mounted and the size of the platform allows its use in MRI scanner bore. Finally, the design helps to further customize the platform to properly match the kinematic requirements discussed earlier.

2.1 Mechanism Design. The detailed mechanical design of ROBOCATHETER is depicted in Fig. 2. Two identical cylindrical mechanisms interconnected vertically form the basic architecture of the robot. Each subsystem consists of a fixed outer ring and a rotating inner ring. The outer cylinder is attached to the casing and hence forms the platform base. A radial bearing at the bottom section of each level makes it possible for the inner rings to rotate with respect to the base. The remaining two DOFs generate

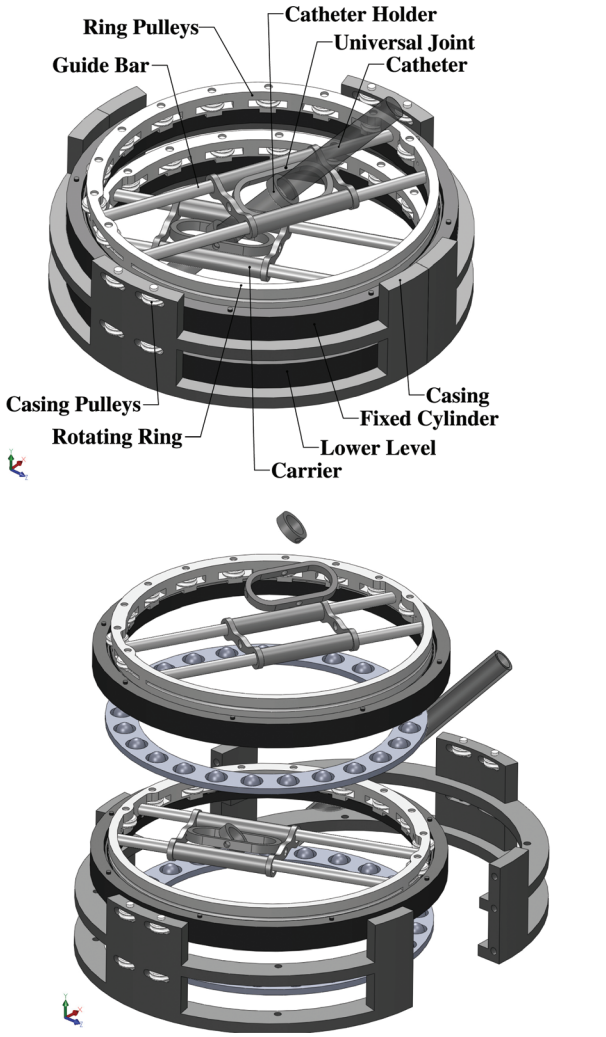

Fig. 2 Parallel mechanism architecture (top), and its expanded view (bottom)

the linear motion for the two carriers sliding over the guide bars. The aforedescribed rotational motions along with the two prismatic DOFs form the desired four active DOFs expected from the mechanism. Each carrier has a universal joint at its center that acts like a liaison between the platform and the catheter. These passively actuated universal joints can eventually place the catheter in any desired orientations. While the distance between the catheter's tip and the lower universal joint is kept constant, the distal end of the catheter is left to move freely with respect to the upper joint.

2.2 Actuation System Design. Placement of the actuators outside the MRI scanner area enables the employment of conventional electric motors to drive the robot joints. However, this arrangement necessitates the development of a power transmission system that allows the remote control of the platform. The transmission system is composed of two closed chains of plastic ropes for each level of the platform. Figure 3 demonstrates the transmission system for one of the levels. Here, r indicates the position of the carrier and θ is the angle of rotation of the ring, with the positive direction shown in Fig. 3. In this configuration, the closed chains numbered 1 and 2 correspond to linear and rotational DOFs, respectively. These chains transmit the power from the DC motors (numbered 5 and 6) to the corresponding connection points on the mechanism (numbered 3 and 4). Different sets of pulleys considered in between (e.g., number 9) not only guide

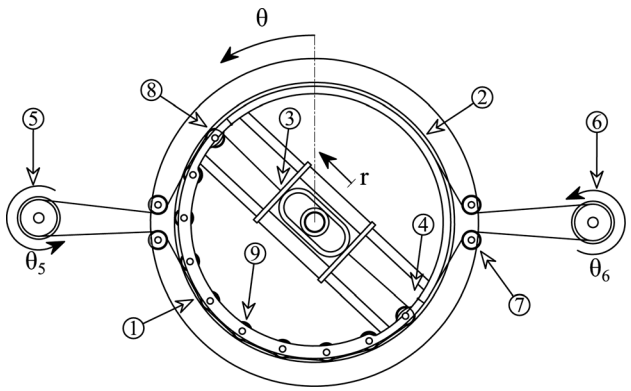

Fig. 3 Transmission system

the cables to pass the desired paths (e.g., numbers 7 and 8) but also significantly reduce friction. It is noted that when the inner ring rotates due to the actuation of motor 6, there is no relative motion between cable 2 and the ring, and hence no friction is created. However, a relative motion between cable 1 and the inner ring occurs when the carrier is actuated by motor 5 or when the ring rotates. Therefore, the movement of this cable is subjected to the friction force. This is the reason why in Fig. 3 the pulleys are arranged only along a semicircle. In order to perform the catheter positioning task, the position of the carriers at each level, that is, the rotation angle of the rotating ring and the displacement of the carrier in the corresponding coordinate system are required. To achieve this, we equipped the motors with encoders attached directly to the motor shafts. Referring to Fig. 3, the encoder attached to motor 6 determines the angle of rotation to be $\theta = (R'/R)\theta_6$, where R' is the radius of the pulley, R is the radius of the rotating ring and θ_6 is the angle of the motor shaft 6 obtained from the encoder data. In addition, the encoder attached to the shaft of motor 5, is used to determine the position of the carrier, i.e., r. Prior to the description of the associated equation, the coupling effect between the two DOFs needs to be investigated. To describe this coupling, we assume in Fig. 3 that motor 5 is locked and that motor 6 rotates counter clockwise. Consequently, cable 1 remains motionless but cable 2 pulls point 4 and rotates the ring. The rotation reduces the tension in cable 1 between point 3 and pulley 8, while the other portion of the cable is tightened. As a result, the carrier tends to move away from pulley 8 as if motor 5 rotated clockwise. The length of dislocation is equal to $r = -R'\theta_6$. Therefore, the encoder signal from motor 5 should be modified to yield the correct displacement of the carrier. The displacement of the carrier in the corresponding coordinate system is calculated to be $r = R'\theta_5 - R'\theta_6$, where θ_5 is the angle of motor shaft 5.

3 Kinematic Equations

In this section, we develop the forward and inverse kinematic equations of the proposed parallel architecture.

3.1 Forward Kinematics of the Parallel Platform. To derive the equations corresponding to the forward kinematics of the proposed mechanism, four different frames as depicted in Fig. 4 are defined: (1) base frame $\{B\}$ which is fixed in the universal coordinate system and its Z-axis is in vertical direction, (2) lower frame $\{L\}$ which is attached to the center point of the lower cylinder with its Z-axis being along the vertical direction and the X-axis coinciding with the lower level linear direction, (3) upper frame $\{U\}$ which is the same as the lower frame except that it is placed at the center point of the upper cylinder with its X-axis being along the upper sliding bar's center line, and (4) end effector base $\{E\}$ which is attached to the catheter's center of mass with its Z-axis being along the catheter long axis. In addition to the aforementioned frames, there are two additional frames $\{UE\}$ and $\{LE\}$ that have the same orientation as $\{U\}$ and $\{L\}$ do but are attached to the universal joint's center points in the upper and lower levels, respectively. For each coordinate system, e.g., $\{B\}$, we denote the unit vectors indicating principal directions by $\hat{\mathbf{X}}_B, \hat{\mathbf{Y}}_B$, and $\hat{\mathbf{Z}}_B$. In addition, ${}^B\mathbf{P}_u$ and ${}^B\mathbf{P}_l$ are two position vectors described in frame $\{B\}$ (left superscript B) that point to the location of catheter carriers in upper (subscript u) and lower (subscript l) levels, respectively. By taking advantage of the relationship between them, the forward kinematics of the system can be described as follows:

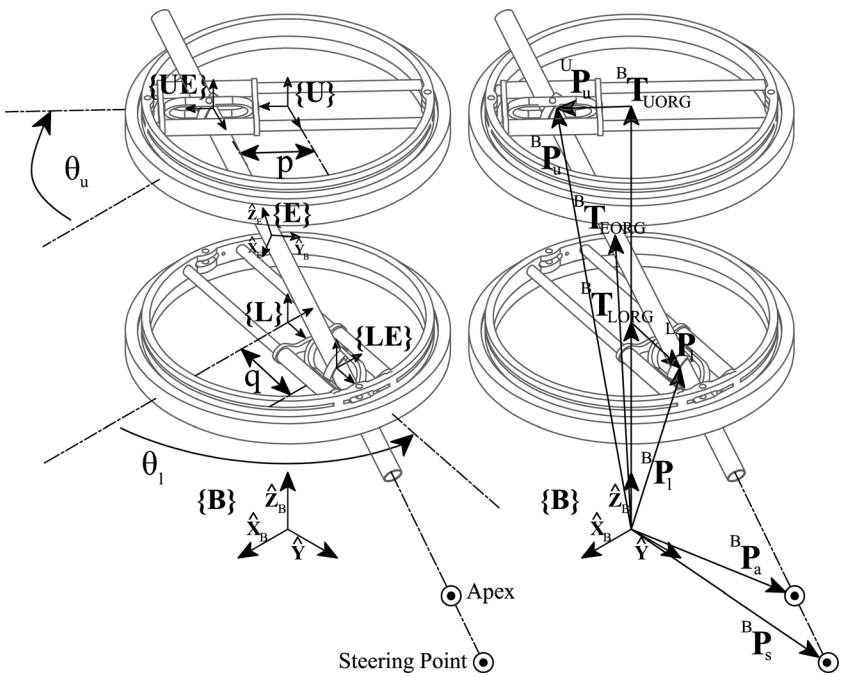

Fig. 4 The coordinate system used in deriving the kinematic equations

$$ {}^{B}\mathbf{P}_u = {}^{B}_{U}R\,{}^{U}\mathbf{P}_\mathbf{u} + {}^{B}\mathbf{T}_{UORG} \tag{1} $$

where ${}^{B}_{U}R$ is a mapping that represents the rotation of $\{U\}$ relative to $\{B\}$ and ${}^{B}\mathbf{T}_{UORG}$ is a vector that represents the origin of frame $\{U\}$ relative to $\{B\}$. From Eq. (1), we have

$$ {}^{B}\mathbf{P}_u = \begin{bmatrix} p\cos\theta_u \\ p\sin\theta_u \\ \|{}^{B}\mathbf{T}_{UORG}\| \end{bmatrix}, \tag{2} $$

where $\|.\|$ indicates the Euclidean norm of a vector, θ_u represents the rotation of the upper cylinder about vertical axis and p is the distance between the carrier and the upper cylinder's center point, where $\{U\}$ is attached. These joint parameters will be actively controlled when the catheter is manipulated. An alternative way to locate the upper tool holder is through the end-effector frame $\{E\}$ using

$$ {}^{B}\mathbf{P}_u = {}^{B}_{E}R\,{}^{E}\mathbf{P}_\mathbf{u} + {}^{B}\mathbf{T}_{EORG} \tag{3} $$

where ${}^{B}_{E}R$ represents the orientation of the catheter, ${}^{E}\mathbf{P}_\mathbf{u}$ is the upper holder position vector in $\{E\}$ and ${}^{B}\mathbf{T}_{EORG}$ is the vector that describes the origin of frame $\{E\}$ relative to $\{B\}$. Substituting for ${}^{E}\mathbf{P}_\mathbf{u}$ and ${}^{B}\mathbf{T}_{EORG}$, results in

$$ {}^{B}\mathbf{P}_u = {}^{B}_{E}Rl\hat{\mathbf{Z}}_\mathbf{E} + \begin{bmatrix} q\cos\theta_l \\ q\sin\theta_l \\ \|{}^{B}\mathbf{T}_{LORG}\| \end{bmatrix} \tag{4} $$

where θ_l and q play the same role as θ_u and p in Eq. (2) except that they are related to the lower level of the platform. In addition, in Eq. (4), l is the length of the catheter between the lower and upper holders that may change with time and ${}^{B}\mathbf{T}_{LORG}$ represents the origin of frame $\{L\}$ relative to $\{B\}$. From Eqs. (2) and (4), we have

$$ {}^{B}_{E}Rl\hat{\mathbf{Z}}_\mathbf{E} = \begin{bmatrix} p\cos\theta_u - q\cos\theta_l \\ p\sin\theta_u - q\sin\theta_l \\ h \end{bmatrix} \tag{5} $$

where $h = \|{}^{B}\mathbf{T}_{UORG}\| - \|{}^{B}\mathbf{T}_{LORG}\|$ is the vertical distance between the upper and lower cylinders. Since any 3×3 rotation matrix can be described by three independent parameters, (5) contains four unknowns including ${}^{B}_{E}R$ and l. Since the catheter does not rotate about its long axis, it only has two rotational DOFs. By choosing a proper representation of its orientation, the number of unknowns in (5) can be reduced to three and hence the forward kinematics problem becomes solvable. The *X-Y-Z* Euler angles representation is used for this purpose [20]. Based on this representation, the final orientation of the catheter is

$$ R_{X'Y'Z'}(\alpha,\beta,0) = \begin{bmatrix} \cos\beta & 0 & \sin\beta \\ \sin\alpha\sin\beta & \cos\alpha & -\sin\alpha\cos\beta \\ -\cos\alpha\sin\beta & \sin\alpha & \cos\alpha\cos\beta \end{bmatrix} \tag{6} $$

Substituting Eq. (6) in Eq. (5) for ${}^{B}_{E}R$ results in

$$ l\sin\beta = p\cos\theta_u - q\cos\theta_l \tag{7a} $$

$$ l\sin\alpha\cos\beta = q\sin\theta_l - p\sin\theta_u \tag{7b} $$

$$ l\cos\alpha\cos\beta = h \tag{7c} $$

Solving the above equations results in the orientation parameters as

$$ \alpha = \arctan\left(\frac{q\sin\theta_l - p\sin\theta_u}{h}\right) \tag{8a} $$

$$ \beta = \arctan\left(\frac{p\cos\theta_u - q\cos\theta_l}{\sqrt{h^2 + (q\sin\theta_l - p\sin\theta_u)^2}}\right) \tag{8b} $$

We denote the apex and steering point shown in Fig. 4 by ${}^{B}\mathbf{P}_a = [x_a, y_a, z_a]^T$ and ${}^{B}\mathbf{P}_s = [x_s, y_s, z_s]^T$. Since the apex and the steering point are in-plane positions of two arbitrarily chosen X-Y planes, among the six parameters of ${}^{B}\mathbf{P}_a$ and ${}^{B}\mathbf{P}_s$, z_a and z_s can be assumed to be known. By describing the four remaining parameters in terms of joint-space parameters, the forward kinematics of the robot is obtained. Starting with the apex we have

$$ {}^{B}\mathbf{P}_a = {}^{B}\mathbf{P}_l + n\begin{bmatrix} c\beta & 0 & s\beta \\ s\alpha s\beta & c\alpha & -s\alpha c\beta \\ -c\alpha s\beta & s\alpha & c\alpha c\beta \end{bmatrix}\begin{bmatrix} 0 \\ 0 \\ 1 \end{bmatrix} = \begin{bmatrix} q\cos\theta_l \\ q\sin\theta_l \\ \|{}^{B}\mathbf{T}_{LORG}\| \end{bmatrix} + m\begin{bmatrix} s\beta \\ -s\alpha c\beta \\ c\alpha c\beta \end{bmatrix} \tag{9} $$

where the scalar $m = (z_a - \|{}^{B}\mathbf{T}_{LORG}\|)/(\cos\alpha\cos\beta)$. Substituting for α and β from Eq. (8), we obtain

$$ \begin{aligned} x_a &= \frac{h^2 q\cos\theta_l + (z_a - \|{}^{B}\mathbf{T}_{LORG}\|)\left(\sqrt{h^2 + (q\sin\theta_l - p\sin\theta_u)^2}\right)(p\cos\theta_u - q\cos\theta_l)}{h^2} \\ y_a &= \frac{hq\sin\theta_l - (z_a - \|{}^{B}\mathbf{T}_{LORG}\|)(q\sin\theta_l - p\sin\theta_u)}{h} \end{aligned} \tag{10} $$

Substituting z_a with z_s in Eq. (10), the parameters of the steering point ${}^{B}\mathbf{P}_s$, that is, x_s and y_s are determined. These four in-plane coordinates, as well as the known parameters z_a and z_s provide the forward kinematics of the manipulator.

3.2 Inverse Kinematics of the Parallel Architecture. The primary objective in obtaining the inverse kinematics of any robotic platform is to relate the task space with the joint space. This enables the controller to position and orient the end effector by adjusting the joint parameters. To obtain the inverse kinematic equations for the proposed platform, the frame $\{E\}$ attached to the end effector is described based on the positions of the apex ${}^{B}\mathbf{P}_\mathbf{a}$ and steering point ${}^{B}\mathbf{P}_s$. These target points are illustrated in Fig. 4. The principle direction of $\{E\}$ is defined to be

$$\hat{\mathbf{Z}}_E = \frac{{}^B\mathbf{P}_a - {}^B\mathbf{P}_s}{\|{}^B\mathbf{P}_a - {}^B\mathbf{P}_s\|}, \quad \hat{\mathbf{Y}}_E = \frac{\hat{\mathbf{X}}_B \times \hat{\mathbf{Z}}_E}{\|\hat{\mathbf{X}}_B \times \hat{\mathbf{Z}}_E\|}, \quad \hat{\mathbf{X}}_E = \hat{\mathbf{Y}}_E \times \hat{\mathbf{Z}}_E \tag{11}$$

To obtain the joint parameters θ_l and q, the above equations along with the position of the mentioned pair of tracking points are utilized as follows:

$${}^B\mathbf{P}_l = {}^B\mathbf{P}_s + n\hat{\mathbf{Z}}_E \tag{12}$$

where n is the distance between the steering point and the lower career along the end effector. The dot product of Eq. (12) with $\hat{\mathbf{Z}}_B$ results in

$${}^B\mathbf{P}_l \cdot \hat{\mathbf{Z}}_B = {}^B\mathbf{P}_s \cdot \hat{\mathbf{Z}}_B + n\hat{\mathbf{Z}}_E \cdot \hat{\mathbf{Z}}_B \tag{13}$$

Since it is more convenient to express the location of the apex and steering point with respect to a physical reference, it is assumed that the origin of the base frame coincides with the center of the lower level which results in ${}^B\mathbf{P}_l \cdot \hat{\mathbf{Z}}_B = 0$, and hence $n = -({}^B\mathbf{P}_s \cdot \hat{\mathbf{Z}}_B)/(\hat{\mathbf{Z}}_E \cdot \hat{\mathbf{Z}}_B)$. Substituting $\hat{\mathbf{Z}}_E$ from Eq. (11) into Eq. (12) with further simplifications result in

$${}^B\mathbf{P}_l = \frac{{}^B\mathbf{P}_s(\hat{\mathbf{Z}}_B \cdot {}^B\mathbf{P}_a) - {}^B\mathbf{P}_a(\hat{\mathbf{Z}}_B \cdot {}^B\mathbf{P}_s)}{({}^B\mathbf{P}_a - {}^B\mathbf{P}_s) \cdot \hat{\mathbf{Z}}_B} = \frac{\hat{\mathbf{Z}}_B \times ({}^B\mathbf{P}_a \times {}^B\mathbf{P}_s)}{({}^B\mathbf{P}_a - {}^B\mathbf{P}_s) \cdot \hat{\mathbf{Z}}_B} \tag{14}$$

using the fact that $\mathbf{a} \times (\mathbf{b} \times \mathbf{c}) = \mathbf{b}(\mathbf{a} \cdot \mathbf{c}) - \mathbf{c}(\mathbf{a} \cdot \mathbf{b})$. Knowing ${}^B\mathbf{P}_l$, the lower level joint parameters are

$$q = \|{}^B\mathbf{P}_l\| = \left\| \frac{\hat{\mathbf{Z}}_B \times ({}^B\mathbf{P}_a \times {}^B\mathbf{P}_s)}{({}^B\mathbf{P}_a - {}^B\mathbf{P}_s) \cdot \hat{\mathbf{Z}}_B} \right\| \tag{15a}$$

$$\theta_l = \arctan\left(\frac{\dfrac{\hat{\mathbf{Z}}_B \times ({}^B\mathbf{P}_a \times {}^B\mathbf{P}_s)}{({}^B\mathbf{P}_a - {}^B\mathbf{P}_s) \cdot \hat{\mathbf{Z}}_B} \cdot \hat{\mathbf{Y}}_B}{\dfrac{\hat{\mathbf{Z}}_B \times ({}^B\mathbf{P}_a \times {}^B\mathbf{P}_s)}{({}^B\mathbf{P}_a - {}^B\mathbf{P}_s) \cdot \hat{\mathbf{Z}}_B} \cdot \hat{\mathbf{X}}_B} \right) \tag{15b}$$

Similarly for θ_u and p, we obtain

$$p = \|{}^B\mathbf{P}_u\| = \left\| \frac{h({}^B\mathbf{P}_a - {}^B\mathbf{P}_s) + \hat{\mathbf{Z}}_B \times ({}^B\mathbf{P}_a \times {}^B\mathbf{P}_s)}{({}^B\mathbf{P}_a - {}^B\mathbf{P}_s) \cdot \hat{\mathbf{Z}}_B} \right\| \tag{16a}$$

$$\theta_u = \arctan\left(\frac{\dfrac{h({}^B\mathbf{P}_a - {}^B\mathbf{P}_s) + \hat{\mathbf{Z}}_B \times ({}^B\mathbf{P}_a \times {}^B\mathbf{P}_s)}{({}^B\mathbf{P}_a - {}^B\mathbf{P}_s) \cdot \hat{\mathbf{Z}}_B} \cdot \hat{\mathbf{Y}}_B}{\dfrac{h({}^B\mathbf{P}_a - {}^B\mathbf{P}_s) + \hat{\mathbf{Z}}_B \times ({}^B\mathbf{P}_a \times {}^B\mathbf{P}_s)}{({}^B\mathbf{P}_a - {}^B\mathbf{P}_s) \cdot \hat{\mathbf{Z}}_B} \cdot \hat{\mathbf{X}}_B} \right) \tag{16b}$$

3.3 Singularity Analysis. Singular points are those of task space for which there is no unique solution to the joint parameters to obtain a desired velocity. In order to determine the singular points, we first find the Jacobian matrix which defines a linear mapping between the vector of joint velocities and the vector of end-effector velocities, that is $[\dot{x}_a, \dot{y}_a, \dot{x}_s, \dot{y}_s]^T = J_{4\times4}\left[\dot{q}, \dot{\theta}_l, \dot{p}, \dot{\theta}_u\right]^T$. The set of those parameters for which the matrix J becomes rank-deficient represents singularity. From Eq. (10), the elements of Jacobian matrix is expressed as

$$J_{11} = \frac{z_a - \|{}^B\mathbf{T}_{LORG}\|}{h^2}\left(\frac{(q\sin\theta_l - p\sin\theta_u)(p\cos\theta_u - q\cos\theta_l)\sin\theta_l}{\sqrt{h^2 + (q\sin\theta_l - p\sin\theta_u)^2}} - \cos\theta_l\sqrt{h^2 + (q\sin\theta_l - p\sin\theta_u)^2} \right) + p\cos\theta_l,$$

$$J_{12} = \frac{z_a - \|{}^B\mathbf{T}_{LORG}\|}{h^2}\left(\frac{(q\sin\theta_l - p\sin\theta_u)(p\cos\theta_u - q\cos\theta_l)q\cos\theta_l}{\sqrt{h^2 + (q\sin\theta_l - p\sin\theta_u)^2}} - q\sin\theta_l\sqrt{h^2 + (q\sin\theta_l - p\sin\theta_u)^2} \right) - q\sin\theta_l,$$

$$J_{13} = \frac{z_a - \|{}^B\mathbf{T}_{LORG}\|}{h^2}\left(\frac{-(q\sin\theta_l - p\sin\theta_u)(p\cos\theta_u - q\cos\theta_l)\sin\theta_u}{\sqrt{h^2 + (q\sin\theta_u - p\sin\theta_u)^2}} - \cos\theta_u\sqrt{h^2 + (q\sin\theta_l - p\sin\theta_u)^2} \right),$$

$$J_{14} = \frac{z_a - \|{}^B\mathbf{T}_{LORG}\|}{h^2}\left(\frac{-(q\sin\theta_l - p\sin\theta_u)p\cos\theta_u - q\cos\theta_l)p\cos\theta_u}{\sqrt{h^2 + (q\sin\theta_u - p\sin\theta_u)^2}} - p\sin\theta_u\sqrt{h^2 + (q\sin\theta_l - p\sin\theta_u)^2} \right),$$

$$J_{21} = \left(1 - \frac{z_a - \|{}^B\mathbf{T}_{LORG}\|}{h}\right)\sin\theta_l, \; J_{22} = \left(1 - \frac{z_a - \|{}^B\mathbf{T}_{LORG}\|}{h}\right)q\cos\theta_l,$$

$$J_{23} = \frac{z_a - \|{}^B\mathbf{T}_{LORG}\|}{h}\sin\theta_u, \; J_{24} = \frac{z_a - \|{}^B\mathbf{T}_{LORG}\|}{h}p\cos\theta_u \tag{17}$$

and $J_{31}, J_{32}, J_{33}, J_{34}$ and $J_{41}, J_{42}, J_{43}, J_{44}$ are obtained by substituting z_a with z_s in Eq. (17), respectively. It is apparent that for $q = 0$, second column of J becomes zero and its rank decreases. Similarly, for $p = 0$, the forth column is zero and reduces the rank of J. Thus, singularity takes place when a carrier passes through the center of the corresponding ring, wherein there are infinitely many solutions to the angular joint parameters. To examine if there are any other combinations of joint values resulting in work space singularity, a numerical analysis can be conducted. to this end, we first grid the joint space and then calculate the least singular value of the Jacobian matrix, namely $\underline{\sigma}(J)$. At each point where this quantity is zero, the rank of the Jacobian matrix is not full and that position denotes a singularity. Since we have four parameters, namely p, q, θ_l, and θ_u, in order to demonstrate this analysis, we plot $\underline{\sigma}(J)$ with respect to p and q while at each point a 2D search over θ_l and θ_u has completed. Figure 5 shows the numerical result and indicates that only for $p = 0$ or $q = 0$ singularity happens.

4 Experimental Result

Figure 6 (left) shows the experimental setup built to evaluate the system performance. Figure 6 (top-right) is the designed mechanism to adjust the tension in the platform. In this mechanism, there are two sets of fixed and mobile pulleys for each level. The latter one slides through a slot to loosen or tighten the nylon cable so that the appropriate tension can be achieved. Figure 6 (bottom-right) shows the mounting of the DC motor in this platform. In this setup, we use four DC motors to fully actuate the platform. The shafts of the motors are attached to the pulleys by means of couplers. The cables are wrapped around the pulleys twice to avoid slippage. DC motor encoders are utilized to measure the position of the shafts. In this setup, we use dSPACE as real-time control and data acquisition system. We consider residual masses added on the distal end of the catheter to examine the performance of the controlled system in the presence of additional weights on top of the catheter. This weights represent a module that will be later used to insert the catheter inside the left ventricle and to handle the bending section. The cables used are nylon

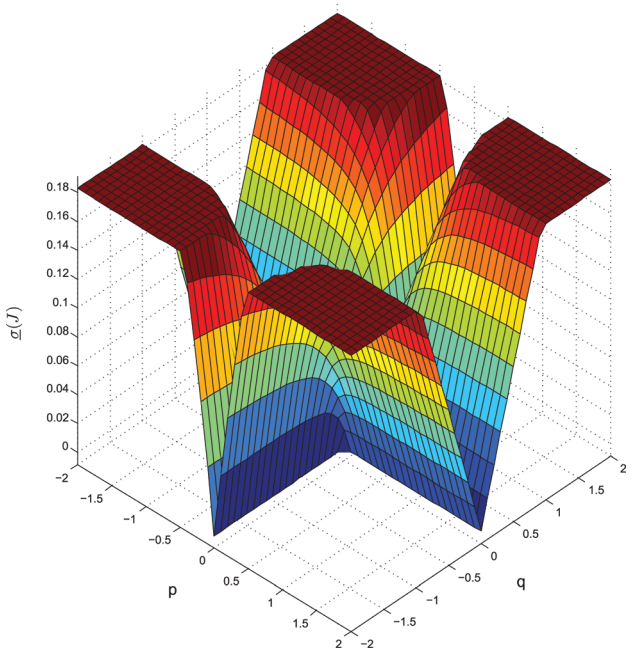

Fig. 5 Jacobian matrix sensitivity analysis

fishing lines, 1 mm in diameter and with Young modulus of 5 GPa. To adjust the pretension value and estimate the dynamic tension in the cables, fiber optic sensors are used, where the data from an optical sensor interrogator, built in-house, is logged and analyzed in LABVIEW. Considering the stress–strain relation for plastic strings, this data are converted into force and used to calculate the tension in the cables.

4.1 Evaluation of the Design and Set Point Tracking. In this section, we evaluate the performance of the system. First, the step response of the system is examined. To simplify the interpretation of the plots in this section, the step responses shown here refer to the cases, where the lower level of the platform is kept motionless and the orientation of the catheter is varied by actuating the upper carrier's linear DOF. In this experiment, an extra masses of 1 kg is added on top of the catheter to account for the equipments/tools that will be installed on top of the end effector. By adding residual masses on top of the catheter, the system nonlinearities become more obvious. In fact, the transient response of the platform changes according to the angle that catheter makes with the vertical axis. Due to this nonlinear behavior, we found that it is not feasible to have a single set of PID control gains that can guarantee the desired performance over all the operating conditions, as well as all the desired set points. The results of this case study suggest that in order to obtain the desired performance over a range of set points and operating conditions, different sets of PID gains should be tuned. To this aim, the distance of the holder from the origin is segmented into six regions and a look up table is developed to schedule the PID gains associated with each segment. Shown in Fig. 7 is the system response using a PID controller with variable gains.

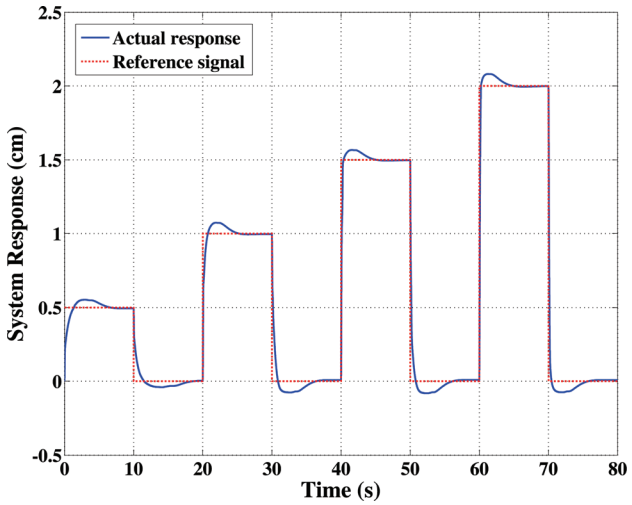

Fig. 7 Response of the system with a residual mass

4.2 Trajectory Tracking. In order to evaluate the effectiveness of the system in providing the task space required for aortic

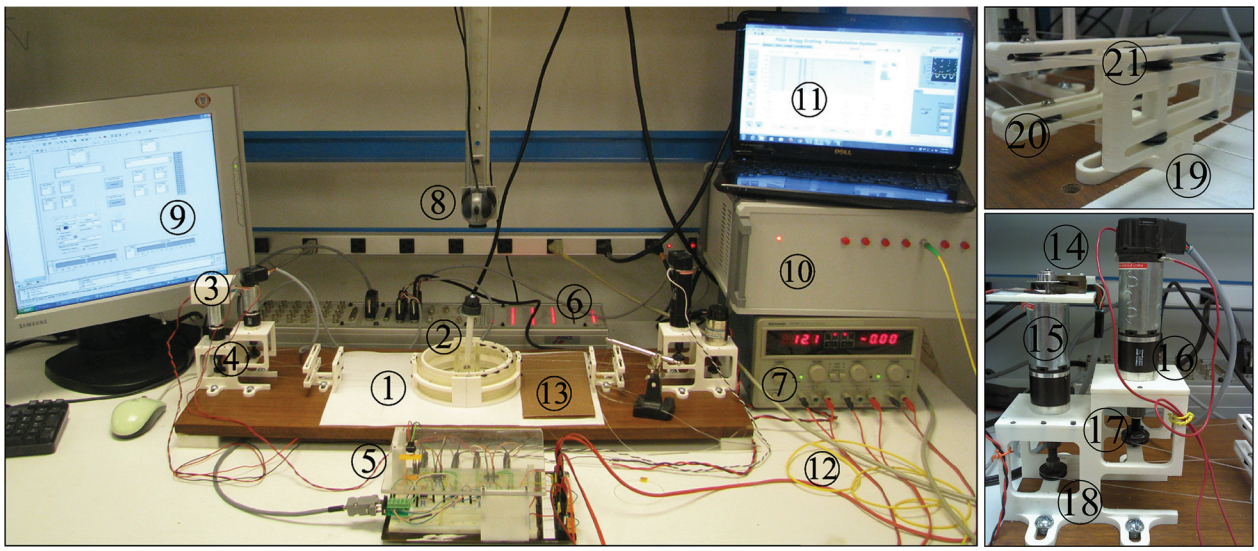

Fig. 6 Experimental setup including: (1) platform, (2) marker/mass weight, (3) DC motors, (4) transmission system, (5) motor driver board, (6) dSPACE real-time control and data acquisition system, (7) power supply, (8) camera, (9) control desk, (10) optical sensor interrogator, (11) LabView interface, (12) fiber optic sensors bundle, (13) sensor-cable connection point (14) optical encoder (15) DC motor (16) gearbox (17) coupler and pulley (18) stand (19) tension adjustment mechanism (20) sliding pulley, and (21) fixed pulley

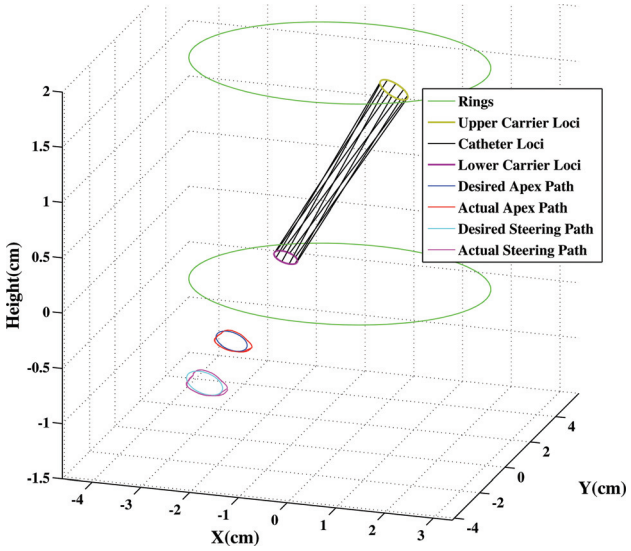

Fig. 8 End effector loci

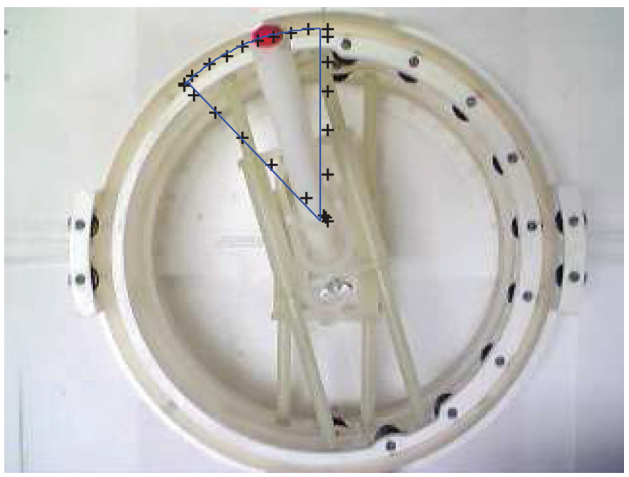

Fig. 9 Trajectory tracking using image feedback

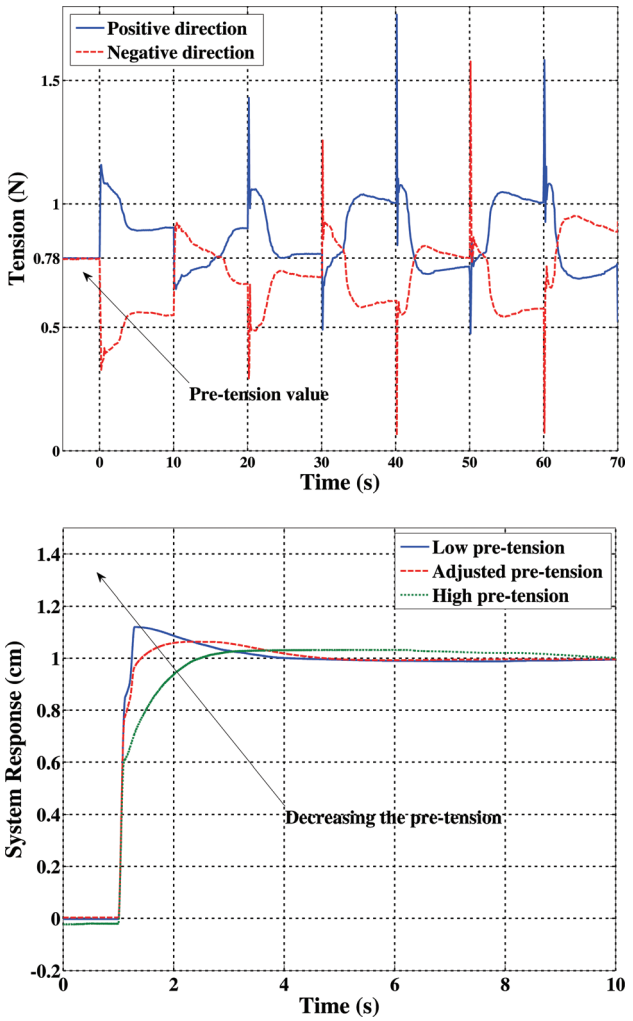

Fig. 10 Tension in the cables (top plot); system response for different pretensions (bottom plot)

valve implantation in beating-heart interventions, the performance of the controlled system to track reference trajectories is examined here. In a typical motion control problem, two reference inputs for the steering point and apex are given, from which the corresponding trajectories for each joint is determined uniquely by means of inverse kinematics. Next, by actuating the joints, the end effector is steered so that the desired motion is generated. In the first test, we directly use the motor encoders to measure the joints coordinations. Figure 8 demonstrates the reference and actual task space traveled by the robot in an arbitrary mission. It is noted that in this experiment, the left and right actuation systems are placed about 1 m away from the robot to demonstrate the ability of the system to operate with long cables. The maximum tracking error is computed to be 1.7 mm in the apex path and 1.8 mm in the steering path. While in this experiment we measure the encoder signals as the feedback signal, in the second test we use the image data to mimic the use of MR imaging in a real intervention. To this aim, a red spot is attached on top of the end effector and a camera is installed over the test bed. To minimize the image noise, the background of the robot is covered with white sheet. The online image processing algorithm identifies the colored point in the scene and sends that data as the feedback signal. Since the camera frame per second is low (15 fps), a low speed test is executed. Unlike the first test, we assume that reference trajectory corresponds to the tip of the end effector. Additionally, in order to have a unique motion, we fix the lower level at the origin. The result of this experiment is shown in Fig. 9, where a sector is traveled. The maximum error in this mission is computed to be 1.5 mm.

4.3 Tension Adjustment. One of the parameters that influences the performance of the cable-driven robotic systems is the value of pretension in the cables. The selection of this parameter affects the system response, as well as the control effort, and hence it should be carefully adjusted to ensure an optimized performance. To test the designed mechanism, we performed additional experiments, where fiber optic sensors were attached to the cables as discussed earlier to measure the tension. Figure 10 (top) shows the variation in the cable tension while set point tracking is being sought as in Fig. 10 (bottom). During the actuation period, the tension increases in the portion of the cable that is pulled and reduces in the opposite side of the cable. Since no portion of the cables should be left with zero tension, our first conclusion about pretension adjustment is that it should be set such that the dynamic tension never drops to zero. In other words, the profile shown in Fig. 10 (top) should never cross zero. While this constraint leads to a lower bound on the pretension value, an upper bound can be determined by analyzing the response for pretension values, above which undesired effects are observed. Figure 10 (bottom) illustrates the transient response of the platform under different tension adjustments. Exceeding the upper bound tension leads to a longer settling time and also increases the steady-state

error. Therefore, the initial tension should be set to a value between the two bounds such that the requirements discussed above are met. We set the pretension to 0.8 N.

5 Conclusion and Future Work

Medical interventions under beating-heart condition through a trans-apical approach offer several advantages including the patient's faster recovery compared to the traditional procedures. However, several issues including the dynamically moving workspace need to be carefully addressed to achieve the desired outcomes. In this paper, we propose the design of a robotic platform that could fit the requirements of those sophisticated and minimally-invasive interventions. Being equipped with MRI as the imaging modality, ROBOCATHETER is capable of positioning and orienting the cardiac catheter to avoid collision between the interventional tool and the internal organs under beating-heart condition. Operational needs such as MRI-compatibility, chest relative motion compensation, accuracy, and compactness are addressed in the design of the platform. The experiments collectively illustrate the effectiveness of a variable-gain PID controller in canceling out the coupling and providing reference input tracking. The effectiveness of the proposed design in spanning the task space needed for aortic valve implantation in beating-heart interventions is successfully confirmed through a trajectory tracking experiment.

Acknowledgment

This work was supported by the National Science Foundation under Grant CNS-0932272. All opinions, findings, conclusions or recommendations expressed in this work are those of the authors and do not necessarily reflect the views of the sponsor.

References

[1] Cole, G., Harrington, K., Su, H., Camilo, A., Pilitsis, J., and Fischer, G., 2010, "Closed-Loop Actuated Surgical System Utilizing Real-Time In-Situ MRI Guidance," 12th International Symposium on Experimental Robotics-ISER, pp. 2489–2495.

[2] Su, H., Cole, G., and Fischer, G., 2012, "High-Field MRI-Compatible Needle Placement Robots for Prostate Interventions: Pneumatic and Piezoelectric Approaches," Adv. Robo. Virtual Reality, **26**, pp. 3–32.

[3] Atluri, P., Kozin, E., Hiesinger, W., and Joseph Woo, Y., 2009, "Off-Pump, Minimally Invasive and Robotic Coronary Revascularization Yield Improved Outcomes Over Traditional On-Pump CABG," Int. J. Med. Robot. Comput. Assisted Surg., **5**(1), pp. 1–12.

[4] Li, M., Mazilu, D., and Horvath, K., 2008, "Robotic System for Transapical Aortic Valve Replacement With MRI Guidance," Medical Image Computing and Computer-Assisted Intervention–MICCAI 2008, pp. 476–484.

[5] Li, M., Kapoor, A., Mazilu, D., and Horvath, K., 2011, "Pneumatic Actuated Robotic Assistant System for Aortic Valve Replacement Under MRI Guidance," IEEE Trans. Biomed. Eng., **58**(2), pp. 443–451.

[6] Yeniaras, E., Lamaury, J., Deng, Z., and Tsekos, N. V, 2010, "Towards a New Cyber-Physical System for MRI-Guided and Robot-Assisted Cardiac Procedures," Information Technology and Applications in Biomedicine (ITAB), 2010 10th IEEE International Conference on, pp. 1–5.

[7] Salimi, A., Mohammadpour, J., Grigoriadis, K., and Tsekos, N., 2011, "Dynamic Simulation of Blood Flow Effects on Flexible Manipulators During Intra-Cardiac Procedures on the Beating Heart," Volume 2, Power and Motion Control, Proceedings of ASME Dynamic Systems and Control Conference, Arlington, VA. October 31–November 2, 2011, Paper No. DSCC2011-6167, pp. 487–494.

[8] Susil, R., Krieger, A., Derbyshire, J., Tanacs, A., Whitcomb, L., Fichtinger, G., and Atalar, E., 2003, "System for MR Image–Guided Prostate Interventions: Canine Study," Radiology, **228**(3), pp. 886–894.

[9] Kim, D., Kobayashi, E., Dohi, T., and Sakuma, I., 2002, "A New, Compact MR-Compatible Surgical Manipulator for Minimally Invasive Liver Surgery," Proceedings Medical Image Computing and Computer-Assisted Intervention (MICCAI), pp. 99–106.

[10] Muntener, M., Patriciu, A., Petrisor, D., Mazilu, D., Bagga, H., Kavoussi, L., Cleary, K., and Stoianovici, D., 2006, "Magnetic Resonance Imaging Compatible Robotic System for Fully Automated Brachytherapy Seed Placement," Urology, **68**(6), pp. 1313–1317.

[11] Tsekos, N., Khanicheh, A., Christoforou, E., and Mavroidis, C., 2007, "Magnetic Resonance-Compatible Robotic and Mechatronics Systems for Image-Guided Interventions and Rehabilitation: A Review Study," Annu. Rev. Biomed. Eng., **9**, pp. 351–387.

[12] Stoianovici, D., Song, D., Petrisor, D., Ursu, D., Mazilu, D., Mutener, M., Schar, M., and Patriciu, A., 2007, "MRI Stealth Robot for Prostate Interventions," Minim. Invas. Ther. Appl. Technol., **16**(4), pp. 241–248.

[13] Hungr, N., Fouard, C., Robert, A., Bricault, I., and Cinquin, P., 2011, "Interventional Radiology Robot for CT and MRI Guided Percutaneous Interventions," Medical Image Computing and Computer-Assisted Intervention (MICCAI), pp. 137–144.

[14] Ramezanifar, A., Salimi, A., Mohammadpour, J., Kilicarslan, A., Grigoriadis, K., and Tsekos, N., 2011, "Linear Parameter Varying Control of a Robot Manipulator for Aortic Valve Implantation," Proceedings of ASME Dynamic Systems and Control Conference, Arlington, VA, Vol. 2, October 31–November 2, 2011, Paper No. DSCC2011-6186, pp. 121–127.

[15] Salimi, A., Ramezanifar, A., Mohammadpour, J., Grigoriadis, K., and Tsekos, N., 2012, "ROBOCATH: A Patient-Mounted Parallel Robot to Position and Orient Surgical Catheters," Proceedings of ASME Dynamic Systems and Control Conference, Fort Lauderdale, FL, Vol. 3, October 17–19, 2012, Paper No. DSCC2012-MOVIC2012-8846, pp. 471–480.

[16] Salimi, A., Ramezanifar, A., Mohammadpour, J., and Grigoriadis, K., 2013, "Development of Master-Slave Robotic Systems for MRI-Guided Intracardiac Interventions," Proceedings of ASME Dynamic Systems and Control Conference, Palo Alto, CA, Oct. 21–23, 2013.

[17] Salimi, A., Ramezanifar, A., Mohammadpour, J., and Grigoriadis, K., 2013, "Gain-scheduling Control of a Cable-Driven MRI-Compatible Robotic Platform for Intracardiac Interventions," Proceedings of American Control Conference (ACC), pp. 746–751.

[18] Schauer, D., Hein, A., and Lüth, T., 2003, "Robopoint—An Autoclavable Interactive Miniature Robot for Surgery and Interventional Radiology," International Congress Series, Elsevier, Vol. 1256, pp. 555–560.

[19] Schauer, D., Hein, A., and Lüth, T., 2003, "Dynamic Force Control for a Miniaturized Medical Robot System," Proceedings of IEEE/ASME International Conference on Advanced Intelligent Mechatronics, July, 20–24, 2003, Vol. 2, pp. 1090–1095.

[20] Craig, J., 2004, Introduction to Robotics: Mechanics and Control, 3rd ed, Prentice Hall, NJ.